



Parasitic folds with wrong vergence: How pre-existing geometrical asymmetries can be inherited during multilayer buckle folding



Marcel Frehner*, Timothy Schmid

Geological Institute, ETH Zurich, Switzerland

ARTICLE INFO

Article history:

Received 20 October 2015

Received in revised form

2 March 2016

Accepted 5 April 2016

Available online 9 April 2016

Keywords:

Parasitic folds

Buckle folds

Fold vergence

Asymmetric folds

Structural inheritance

Finite-element method

ABSTRACT

Parasitic folds are typical structures in geological multilayer folds; they are characterized by a small wavelength and are situated within folds with larger wavelength. Parasitic folds exhibit a characteristic asymmetry (or vergence) reflecting their structural relationship to the larger-scale fold. Here we investigate if a pre-existing geometrical asymmetry (e.g., from sedimentary structures or folds from a previous tectonic event) can be inherited during buckle folding to form parasitic folds with wrong vergence. We conduct 2D finite-element simulations of multilayer folding using Newtonian materials. The applied model setup comprises a thin layer exhibiting the pre-existing geometrical asymmetry sandwiched between two thicker layers, all intercalated with a lower-viscosity matrix and subjected to layer-parallel shortening. When the two outer thick layers buckle and amplify, two processes work against the asymmetry: layer-perpendicular flattening between the two thick layers and the rotational component of flexural flow folding. Both processes promote de-amplification and unfolding of the pre-existing asymmetry. We discuss how the efficiency of de-amplification is controlled by the larger-scale fold amplification and conclude that pre-existing asymmetries that are open and/or exhibit low amplitude are prone to de-amplification and may disappear during buckling of the multilayer system. Large-amplitude and/or tight to isoclinal folds may be inherited and develop type 3 fold interference patterns.

© 2016 Elsevier Ltd. All rights reserved.

1. Introduction

Parasitic folds are very characteristic features in geological multilayer buckle folds and are treated in almost every traditional and modern structural geology text book (Fossen, 2010; Price and Cosgrove, 1990; Ramsay and Huber, 1987; Twiss and Moores, 2007). During polyharmonic folding (Ramsay and Huber, 1987), different wavelengths are established by layers of different thicknesses (according to Biot's dominant wavelength theory; Adamuszek et al., 2013; Biot, 1961; Fletcher, 1977) resulting in folds with smaller wavelength situated within folds with larger wavelength. The folds with smaller wavelength are termed parasitic folds or second-order folds (as opposed to the first-order folds with larger wavelength).

Parasitic folds develop simultaneously with the larger fold; hence they share the same (or similar) fold axis orientation and

axial plane orientation as the larger fold. This similarity of style and attitude of different fold orders are known as the Pumpelly's rule that emphasizes the "general parallelism which exists between the minute and general structure", an observation that Pumpelly et al. (1894) made in the Green Mountains in Massachusetts. As a result, parasitic folds exhibit a characteristic asymmetry (or fold vergence), often referred to as S- and Z-shape on either limb of the larger fold and symmetric M-shape close to the hinge of the larger fold. Until De Sitter (1958) introduced the term parasitic fold, such second-order folds were also referred to as drag folds (Ramberg, 1963; Williams, 1961).

The development of parasitic folds has been studied analytically (Hunt et al., 2001; Ramberg, 1964, 1963; Treagus and Fletcher, 2009), as well as in analog (Ramberg, 1964, 1963) and numerical models (Frehner and Schmalholz, 2006). All these studies agree that parasitic folds develop by a combination of buckle folding on two different length scales. When a multilayer stack experiences layer-parallel shortening, all layers start to buckle; but the thin layers develop finite amplitudes prior to the thicker layers and develop short-wavelength symmetric folds (Frehner and

* Corresponding author. Geological Institute, NO E3, ETH Zurich, Sonneggstrasse 5, Switzerland.

E-mail address: marcel.frehner@erdw.ethz.ch (M. Frehner).

Schmalholz, 2006). These folds are then sheared into an asymmetric geometry (S- and Z-folds; following Pumpelly's rule) on the limbs of larger-wavelength folds, which develop finite amplitudes slightly later. In the hinge area of these larger folds, shearing is less marked and the parasitic folds remain symmetric (M-folds; Frehner and Schmalholz, 2006). Even studies not specifically focusing on the development of parasitic folds reproduced this two-stage development in multilayer folds (Schmalholz and Schmid, 2012).

Pumpelly's rule seems to be axiomatic. Van der Pluijm and Marshak (2004) wrote: "In any case, remember that a pattern of fold vergence opposite to that in Figure 10.16 (a "Christmas-tree" geometry) cannot be produced in a single fold generation (Figure 10.17). In fact, this geometry is diagnostic of the presence of at least two fold generations." Indeed, an alleged wrong fold vergence in geological field studies is usually used to argue for two distinct tectonic folding phases. For example, Froitzheim et al. (1994) observed folds on the decameter-scale in the Silvretta nappe (Austroalpine basement; SE Switzerland) that have the wrong vergence for their position within the Ducan synform and Pleuger et al. (2008) observed outcrop-scale folds in the Monte Rosa nappe (Middle Penninic basement; NW Italy) that have the wrong vergence for their position within the Vanzone antiform. In the first case, Froitzheim et al. (1994) interpreted the observed folds to originate from an earlier deformation phase than the larger-scale synform; in the second case, Pleuger et al. (2008) interpreted the observed folds to be younger than the larger-scale antiform. Similarly, Duncan (1984) interpreted minor folds with wrong vergence in the Thor-Odin gneiss dome (Shuswap metamorphic complex, Canadian Cordillera) to originate from a later deformation phase than the larger-scale Pingston fold.

Harrison and Falcon (1934) demonstrated that orogen-perpendicular gravitational collapse can result in a wrong vergence of second-order folds. However, this explanation was suggested for massive limestone formations and is not applicable to the examples above. Llorens et al. (2013b) demonstrated that higher-viscous layers oriented obliquely in a ductile shear zone can develop different vergences during a single simple-shear deformation event or even unfold completely while other layers remain folded. However, their numerical simulations mimic ductile shear zones and not smaller-scale parasitic folds within a larger-scale fold structure and are therefore not directly applicable to the problem at hand.

Here we present a feasibility study to investigate if second-order folds with wrong vergence can occur in multilayer buckle folds generated during only one single deformation phase. In particular, we test if a pre-existing small-scale asymmetry in the multilayer stack (e.g., from non-planar sedimentation and diagenesis) can survive the buckling process and can therefore be inherited as an asymmetric fold with wrong vergence. To test this, we apply a 2D finite-element model to simulate multilayer buckle folding of Newtonian materials.

2. Numerical method and setup

We use the same numerical model that has been explained in detail and successfully benchmarked in Frehner and Schmalholz (2006) and Frehner (2011). The method is based on the finite-element spatial discretization method (Zienkiewicz and Taylor, 2000) using triangular T7/3 isoparametric elements (Cuvellier et al., 1986). The model solves the Stokes equations in 2D plane-strain formulation in the absence of gravity coupled with an incompressible linear viscous (Newtonian) rheology; hence we model the slow viscous deformation governing buckle folding. We use perfectly body-fitting Lagrangian meshes, which allow modeling sharp viscosity jumps across interfaces between individual layers of the multilayer stack (Deubelbeiss and Kaus, 2008).

2.1. Model setup

The initial model setup and boundary conditions are depicted in Fig. 1 and detailed values for the model setup are provided in Table 1. The model consists of three high-viscosity layers (viscosity η_L) intercalated with a low-viscosity matrix (viscosity η_M). The two outer layers have equal thickness, H_0 , and a distance to each other of also H_0 . Sandwiched between them, the third layer is ten times thinner (thickness $h_0 = 0.1 \times H_0$). All model dimensions are normalized using the thickness of the thick layers (i.e., $H_0 = 1$); all model viscosities are normalized using the matrix viscosity (i.e., $\eta_M = 1$) (Table 1).

To initiate buckling of the two thicker layers, we impose a sinusoidal initial geometry on their interfaces according to

$$y_i(x) = -A_{\text{outer}} \sin\left(\frac{2\pi x}{\lambda_d}\right) + c_i, \quad (1)$$

where $y_i(x)$ is the y-coordinate (as a function of the x-coordinate) of the i th interface (i.e., bottom and top interface of the bottom and top thick layer), A_{outer} is the amplitude of the sinusoidal geometry, and c_i is a constant value chosen for each interface such that the layers have the desired thickness and distance to each other. The wavelength of the sinusoidal initial geometry, λ_d , corresponds to the dominant wavelength of the two-layer system (i.e., neglecting the thin central layer) according to Schmid and Podladchikov (2010):

$$\lambda_d = 2\pi H_0 \left(\frac{2\eta_L}{6\eta_M}\right)^{1/3}. \quad (2)$$

Note that the x-axis origin is located at the inflexion point of the outer thick layers (Fig. 1) to be consistent with Equation (1) and the

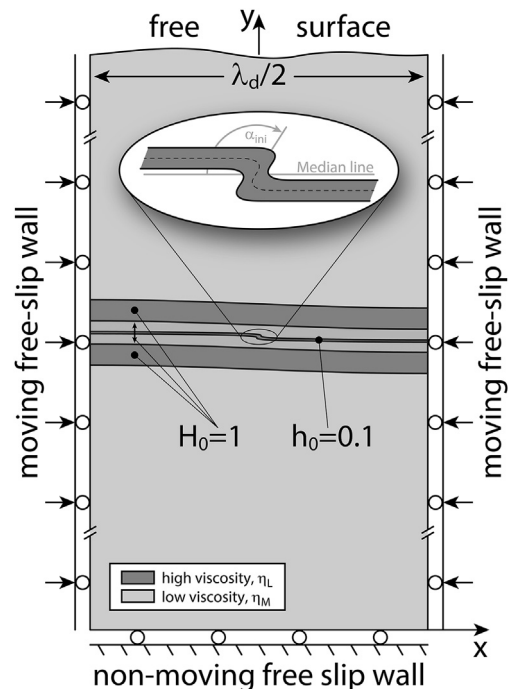


Fig. 1. Sketch (not to scale) of the 2D numerical model setup. A 3-layer system is intercalated with a background matrix of low viscosity. The distance between the two outer layers is equal to their individual thickness, H_0 . The central layer with a 10-times smaller thickness, h_0 , is sandwiched between them. The zoom shows the initial asymmetry of the central layer with the initial skew angle α_{ini} . Note that the x-axis origin is located in the model center.

Table 1
Parameters used to set up the numerical simulations.

Description	Parameter and value
Thickness of outer layers	$H_0 = 1$ (value for normalizing lengths)
Viscosity of matrix	$\eta_M = 1$ (value for normalizing viscosities)
External horizontal strain rate	$\dot{\epsilon}_{bg} = -1$ (value for normalizing strain rates)
Thickness of central layer	$h_0 = 0.1$
Viscosity of higher-viscosity layers	$\eta_L = 100$ (Figs. 2–9 and 11)
	$\eta_L = 20$ (Fig. 10)
Resulting dominant wavelength	$\lambda_d = 20.2$ (for $\eta_L = 100$; Figs. 2–9 and 11)
	$\lambda_d = 11.8$ (for $\eta_L = 20$; Fig. 10)
Initial amplitude of outer layers	$A_{outer} = 10^{-4}$ (for $\eta_L = 100$; Fig. 2–9 and 11)
	$A_{outer} = 10^{-2}$ (for $\eta_L = 20$; Fig. 10)
Initial amplitude of central layer	$A_0 = 0.1$
Asymmetry parameters k	$k = 1$
Asymmetry parameter v and resulting initial skew angle α_{ini}	$v = 0.513, 0.713, 0.828, 0.886, 0.944$ $\alpha_{ini} = 15^\circ, 30^\circ, 60^\circ, 90^\circ, 120^\circ$
Asymmetry shift parameter s	$s = 0, 3.4 \left(\frac{1}{3} \frac{\lambda_d}{2}\right), 5.1 \left(\frac{1}{2} \frac{\lambda_d}{2}\right), 6.7 \left(\frac{2}{3} \frac{\lambda_d}{2}\right)$
Distance between two thick layers	H_0 (Figs. 2–8 and 10)
	$1.5 \times H_0, 2 \times H_0, 3 \times H_0$ (Fig. 9)
Amplitude of random red noise on central layer	$A_r = 0.02$

following Equation (3).

2.2. Initial asymmetry

To impose the pre-existing asymmetrical perturbation to the two interfaces of the thin central layer, we made use of the error function (erf), which allows prescribing a single well-determined asymmetric shape at a specific location:

$$x_c(t) = t - v \cdot \text{erf}(kt) + s$$

$$y_c(t) = -A_0 \cdot \text{erf}(kt) - \underbrace{A_{outer} \sin\left(\frac{2\pi x_c}{\lambda_d}\right)}_{\text{Large-scale sinusoid}} + c_c, \quad (3)$$

where $x_c(t)$ and $y_c(t)$ are the x- and y-coordinates (as a function of t) of the central line of the central thin layer (dashed line in the zoom in Fig. 1), v and k determine the shape (i.e., sharpness and skew angle α_{ini}) of the asymmetric geometry, s is the position in x-direction at which the asymmetry is centered ($s = 0$: asymmetry centered at middle of the larger fold limb, $s = \lambda_d/4$: asymmetry centered at synformal hinge), and A_0 is the amplitude in y-direction of the asymmetric shape, which we chose to be the same as the layer thickness ($A_0 = h_0 = 0.1$). Parameter t is used for the parametric formulation of Equation (3); its minimum and maximum value is chosen such that $-\lambda_d/4 \leq x_c \leq \lambda_d/4$. Similar as above, c_c is a constant value chosen such that the central thin layer has the desired distance to the two outer layers. We also impose the large-scale sinusoid (Equation (1)) to the y-coordinate of the central thin layer to have a common large-scale geometry for all three layers independent of the asymmetry. The initial skew angle, α_{ini} , of the asymmetric geometry (Fig. 1) can be calculated as

$$\alpha_{ini} = \tan^{-1}\left(\frac{2A_0k}{\sqrt{\pi} - 2vk}\right). \quad (4)$$

Since we fix the parameters A_0 and k , the initial skew angle solely depends on parameter v (Table 1).

Equation (3) prescribe the asymmetric geometry of the central line of the central layer (dashed line in the zoom in Fig. 1). This line is then shifted down (y-direction) and left (x-direction), as well as up and right to define the lower and upper interface of the thin central layer, respectively. The shift up and down is equal to $\pm h_0/2$ to obtain a thin layer thickness of h_0 ; the shift right and left is equal

to $\pm h_0 v^2 / (12A_0)$, which we found suitable by trial-and-error to obtain a quasi-constant layer thickness along the asymmetric initial geometry. In addition to the asymmetric initial geometry, a random red noise is imposed to the y-coordinates of these interfaces and the central line to allow other small-scale folds to develop independently of the prescribed asymmetry. The amplitude of this red noise, A_r , is five times smaller than the amplitude of the asymmetric geometry ($A_r = A_0/5 = 0.02$; Table 1). The initial amplitudes of the thick and thin layers ($A_{outer} = 10^{-4}$, $A_r = 0.02$) roughly correspond to the value found in Frehner and Schmalholz (2006) to be suitable to develop parasitic folds without a pre-existing asymmetry.

2.3. Boundary conditions

In the x-direction, the size of the numerical model accommodates half the dominant wavelength of the two-layer system ($\lambda_d/2$, Equation (1); Fig. 1). This is justified because the two-layer system is assumed to buckle in a periodic manner; hence, for symmetry reasons, modeling only half a wavelength is sufficient. In the y-direction, the bottom and top boundaries are far enough ($>2\lambda_d$) away from the multilayer stack to have a marginal influence of the boundary conditions.

We apply constant-strain rate layer-parallel shortening to deform the multilayer stack. The particular boundary conditions are:

- Left and right boundaries: Moving free-slip boundary conditions (i.e., zero traction plus prescribed boundary-perpendicular velocity). The horizontal (boundary-perpendicular) velocity is adjusted at every time increment to maintain a constant shortening strain rate, $\dot{\epsilon}_{bg}$.
- Bottom boundary: Non-moving free-slip boundary conditions (i.e., zero traction plus zero boundary-perpendicular velocity).
- Top boundary: Free surface boundary conditions (i.e., zero traction plus zero boundary-perpendicular normal stress).

The prescribed horizontal shortening strain rate is used to normalize strain rate values (i.e., $\dot{\epsilon}_{bg} = -1$; Table 1).

2.4. Calculation procedures

The initial finite-element mesh is set up in a way that the central line of the central layer (dashed line in the zoom in Fig. 1) is

explicitly discretized. Thanks to the body-fitting Lagrangian formulation, this line can then easily be tracked during ongoing deformation. On the other hand, the median line between the two outer layers (dashed white line in Fig. 2) is not a material line and is therefore not discretized by the finite-element mesh. For each time step, we calculate this median line between the upper interface of the lower thick layer (interface A) and the lower interface of the upper thick layer (interface B) using the following procedure:

1. Create a single (high resolution) array with x-coordinates, x_m .
2. Loop through all numerical points on interface A.
 - a. For each point (P_A) on interface A, find the closest point (P_B) on interface B.
 - b. Calculate the midpoint (P_C) between P_A and P_B .
3. Linearly interpolate the array of points P_C onto array x_m . Resulting in array $D_l = \{x_m, y_l\}$.
4. Repeat 2 and 3, but switching interfaces A and B. This results in array $D_u = \{x_m, y_u\}$.
5. Calculate the mean y-coordinate $y_m = (y_l/2 + y_u/2)$ for every x-coordinate in array x_m , resulting in the median line $\{x_m, y_m\}$.

For every time step, we can compare the large-scale median line of the thick layers with the central line of the central thin layer, calculate the deviation of the latter from the former, which corresponds to the thin layer amplitude, or calculate the angle between the two, which corresponds to the evolving skew angle.

3. Results

Fig. 2 shows a series of simulation snapshots of a typical numerical finite-element simulation (in this example, $\alpha_{ini} = 60^\circ$, $s = 0$). During the early folding stages (up to ~18% shortening), the

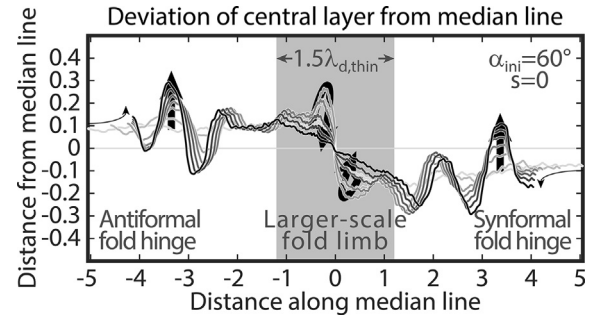


Fig. 3. Deviation of the central thin layer from the larger-scale median line (dashed white line in Fig. 2) as a function of position along the larger-scale fold (abscissa) and shortening for the same simulation as shown in Fig. 2. The amounts of shortening (line gray level) are the same as in the subfigures in Fig. 2 (light gray: initial stage; black: 45% shortening). The left end of the abscissa corresponds to the antiformal hinge, the right end to the synformal hinge, and the figure center to the fold limb of the larger-scale fold. Thin arrows on either end of the figure indicate the shortening of the median line. Bold arrows indicate the amplitude evolution of the thin-layer folds. 1.5 times the dominant wavelength of the thin layer, $\lambda_{d,thin}$, is provided as a gray background.

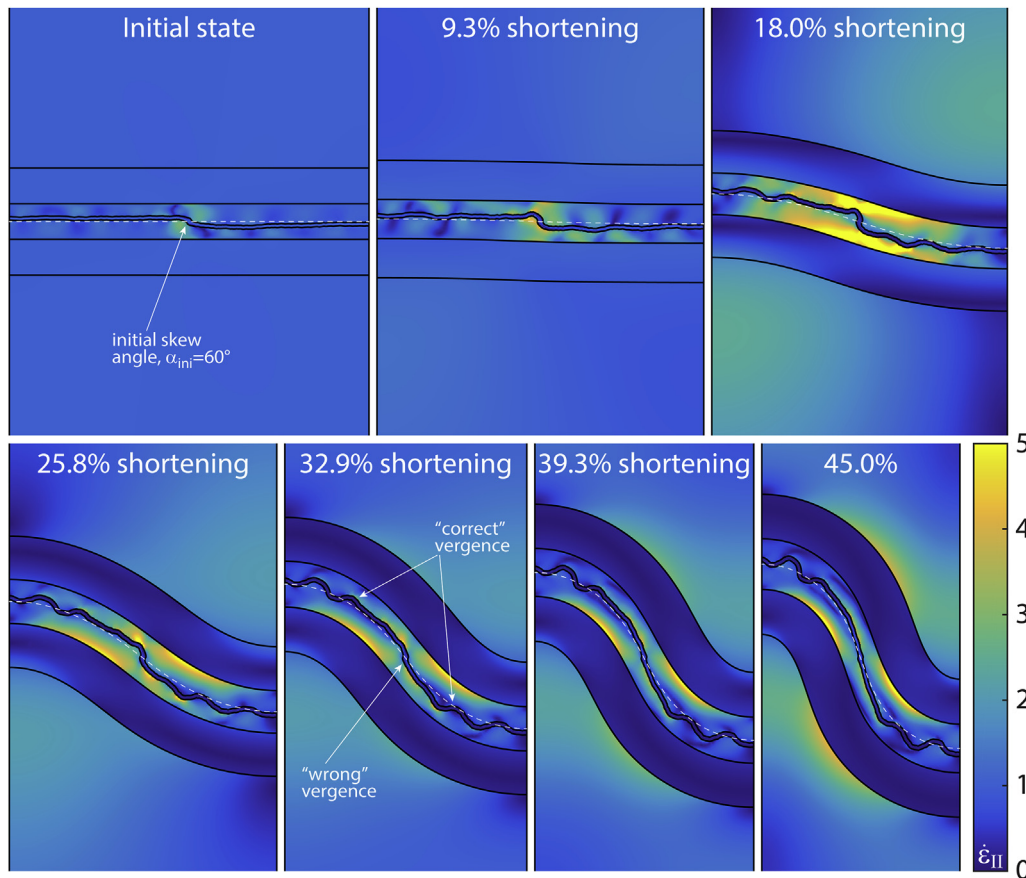


Fig. 2. Simulation snapshots of an example simulation with initial skew angle $\alpha_{ini} = 60^\circ$ and asymmetry shift parameter $s = 0$ (asymmetry centered on the fold limb). Increasing background shortening is indicated in % in each subfigure. Colors correspond to the second invariant of the strain rate tensor, $\dot{\epsilon}_{II}$. The dashed white line corresponds to the larger-scale median line. The initial asymmetry survives the early stages of the buckle folding process, which results in an alleged parasitic fold with wrong vergence, alongside true parasitic folds with correct vergence. (For interpretation of the references to colour in this figure legend, the reader is referred to the web version of this article.)

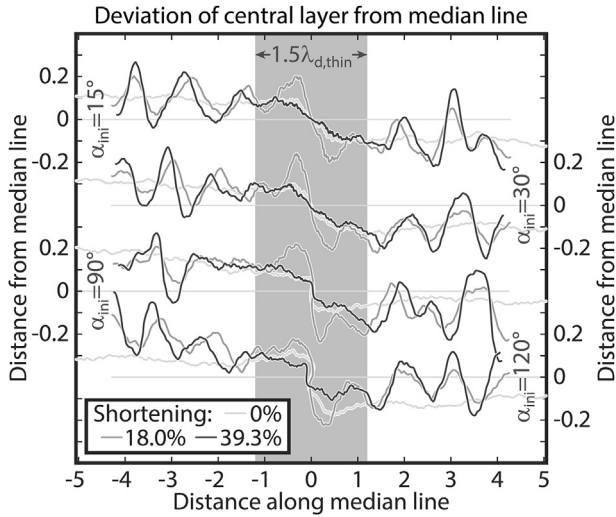


Fig. 4. Same as Fig. 3, but for different initial skew angles, α_{ini} (top to bottom). Compared to Fig. 3, only two amounts of shortening are shown (besides the initial stage), which correspond to the simulation snapshots in Fig. 5.

initial asymmetry amplifies visibly. At the same time, the central thin layer also buckles away from the asymmetry due to the initially imposed random red noise and develops folds with roughly the dominant wavelength, $\lambda_{d,thin} = 2\pi h_0[\eta_L/(6\eta_M)]^{1/3}$ (Biot, 1961). At first (<18% shortening), these buckle folds exhibit an upright symmetric geometry. As soon as the two outer thick layers amplify to finite amplitudes (>18% shortening), the symmetric folds

between the thick layers are sheared into an asymmetric geometry and form typical parasitic folds. This two-stage development of parasitic folds (first symmetric, then sheared into asymmetric geometry) is consistent with the studies of Ramberg (1963) and Frehner and Schmalholz (2006). However, in this study (Fig. 2) the combined amplification of the initial random noise and the initial asymmetry yields parasitic folds with both correct and wrong vergence (at ~32.9% shortening). The initial asymmetry exhibits a Z-shape (clockwise vergence) while the true parasitic folds away from the asymmetry exhibit an S-shape (anticlockwise vergence).

With continuing amplification of the two outer thick layers (>25.8%; Fig. 2), thin-layer folds on the limb of the larger fold generally start to de-amplify. In particular, the pre-existing asymmetry, after initial amplification, de-amplifies and almost vanishes after a shortening of 45%. At the same time, thin-layer folds close to the hinge of the larger fold continue amplifying, which results in well-developed symmetric (M-shaped) parasitic folds.

To better quantify the above observations, Fig. 3 shows the deviation of the central thin layer from the larger-scale median line. The latter is drawn as a dashed white line in Fig. 2. In the center of Fig. 3 (corresponding to the limb of the larger-scale fold), the evolution of the initial asymmetry can be tracked with increasing shortening. The asymmetry first grows up to a shortening of about 18%, after which the asymmetry de-amplifies. Away from the asymmetry, close to the fold hinges, the initial random perturbation develops symmetric buckle folds with the dominant wavelength, $\lambda_{d,thin}$, which continuously amplify during the entire simulation. Similar to the initial asymmetry, those buckle folds closer to the fold limb of the larger-scale fold de-amplify after a certain amount of shortening.

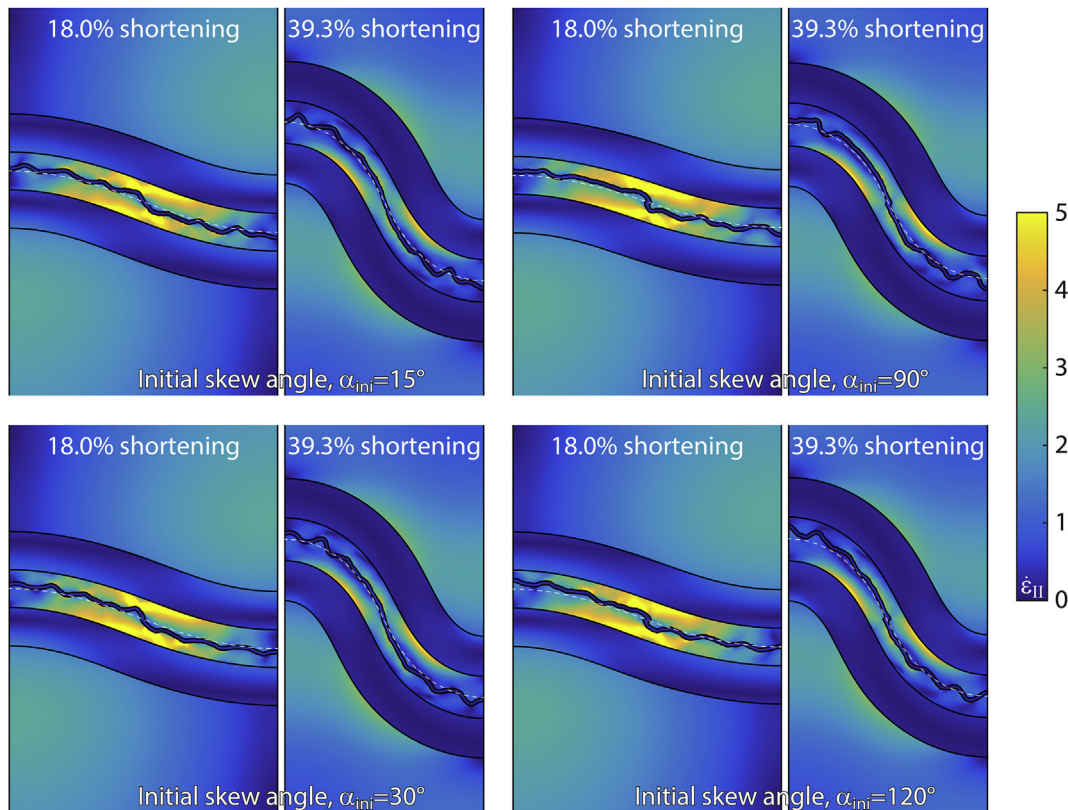


Fig. 5. Simulation snapshots (similar to Fig. 2) of simulations with different initial skew angles, α_{ini} , and asymmetry shift parameter $s = 0$ (asymmetry centered on the fold limb). Compared to Fig. 2, only two snapshots are shown for each initial skew angle.

3.1. Effect of strength of initial asymmetry (skew angle)

To investigate the effect of different strengths of the initial asymmetry, Fig. 4 shows the deviation of the central thin layer from the larger-scale median line for different initial skew angles, $\alpha_{ini} = [15^\circ, 30^\circ, 90^\circ, 120^\circ]$ and Fig. 5 shows the corresponding simulation snapshots, complementing the data and simulation snapshots for $\alpha_{ini} = 60^\circ$ shown in Figs. 3 and 2, respectively. A qualitative comparison does not reveal major differences between the different initial skew angles and observations from Figs. 2 and 3 can be repeated here. All initial asymmetries grow from their initial state up to a shortening of 18% and then de-amplify. In fact, after 39.3% shortening, the amplitude of each asymmetry is comparable to its initial state (Fig. 4). At the same time, close to the larger-scale fold hinges, the thin layer buckles and continuously amplifies to form symmetric (M-shaped) true parasitic folds (Figs. 4 and 5). Parasitic folds closer to the larger-scale fold limb slow down their amplification or even de-amplify with increasing shortening.

The amplitude evolution qualitatively described above is plotted in Fig. 6A as a function of shortening for all the different initial skew angles. We plot the normalized amplitude of the two outer thick layers, calculated from the larger-scale median line (dashed white lines in Figs. 2 and 5), as well as the normalized amplitude of the central thin layer at two localities. On one hand, we calculate the amplitude of the asymmetry as the maximum deviation of the thin-layer from the larger-scale median line within a zone of ± 0.75 dominant wavelengths ($\lambda_{d,thin}$) from the initial asymmetry (gray background in Figs. 3 and 4); on the other hand, we calculate the amplitude of the symmetric (M-shaped) parasitic folds as the maximum deviation of the thin-layer from the larger-scale median line within zones of 1.5 dominant wavelengths ($\lambda_{d,thin}$) away from either larger-scale fold hinge.

While the amplitude of the two outer thick layers grows smoothly (dotted lines in Fig. 6A), the thin-layer amplitudes exhibit minor irregularities and different initial values, which are due to the random noise applied to the thin layer in the initial model setup. Despite these irregularities, Fig. 6A reveals that the initial asymmetry (solid lines in Fig. 6A) grows up to a shortening of about 18% before it de-amplifies and eventually (at ~40% shortening) reaches amplitudes similar to the initial one. The de-amplification begins shortly after the larger-scale fold starts to amplify to finite amplitudes. Close to the larger-scale fold hinges, the symmetric parasitic folds (dashed lines in Fig. 6A) continuously amplify during the entire folding history modeled here.

For comparison, Fig. 6B shows the evolution of the skew angle of the geometrical asymmetry, α , on the same abscissa as Fig. 6A. The skew angle is measured with respect to the larger-scale median line (zoom in Fig. 1). Starting from the initial value, α_{ini} , the skew angle increases up to about 18% shortening in all simulations. In other words, the geometrical asymmetry becomes even more asymmetric and the parasitic fold exhibits an even clearer wrong vergence. The asymmetries with an initial skew angle of $\alpha_{ini} = [60^\circ, 90^\circ]$ reach maximum skew angles larger than 90° ; hence they become overturned folds with respect to the larger-scale median line. When the asymmetry deamplifies ($>18\%$ shortening; Fig. 6A), the skew angle also reduces and reaches the same level of asymmetry as in the initial setup at about 33% shortening. Fig. 6 demonstrates that the geometrical asymmetry not only amplifies and de-amplifies but at the same time also increases and decreases the level of asymmetry. However, the skew angle never becomes negative and the asymmetry therefore never changes its vergence on the larger-scale fold. Negative skew angles would represent the proper vergence for true parasitic folds. Hence, the initial asymmetry keeps its wrong vergence throughout the simulations.

All of the above observations are independent of the initial skew

angle, indicating that the initial skew angle has very little influence on the dynamics of the multilayer system. As a comparison, we also plot in Fig. 6A the amplitude evolution of the two outer thick layers without any thin layer between them (i.e., 2-layer system). The 2-layer system amplifies at a much lower rate compared to all 3-layer systems modeled here, independent of the initial skew angle. In other words, adding the central thin layer with an initial asymmetry strongly modifies the dynamics of the whole multilayer system and lets it amplify much faster.

3.2. Effect of position of initial asymmetry (shift parameter)

To investigate the effect of laterally shifting the initial

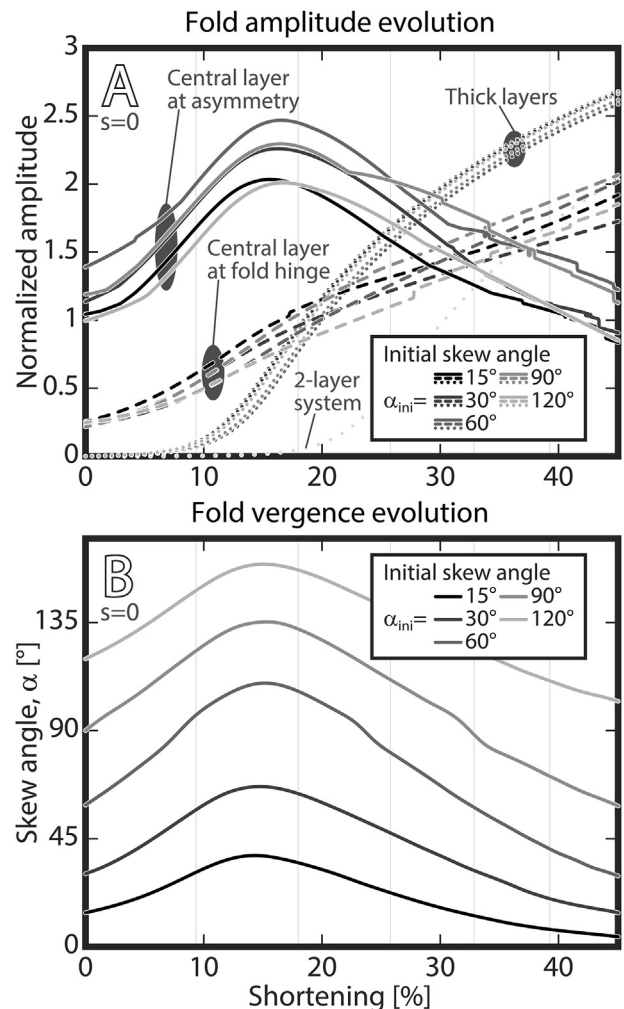


Fig. 6. A) Fold amplitude evolution as a function of increasing shortening for different initial skew angles, α_{ini} (different gray levels) and asymmetry shift parameter $s = 0$. Shown are the amplitude of the larger-scale fold (thick layers; dotted lines), as well as the amplitude of the central thin layer at the larger-scale fold hinge (dashed lines) and at the larger-scale fold limb (i.e., amplitude of the initial asymmetry; solid lines). As a reference, the amplitude evolution of the larger-scale fold is shown for a simulation without any thin layer (2-layer system). All amplitudes are normalized with the initial thickness of the corresponding layer (i.e., thin-layer amplitude normalized with initial thickness of thin layer; thick-layer amplitude normalized with initial thickness of thick layers). B) Evolution of the skew angle, α , of the geometrical asymmetry as a function of increasing shortening for different initial skew angles, α_{ini} , and asymmetry shift parameter $s = 0$. Negative skew angles would represent true parasitic folds with correct vergence; positive skew angles represent parasitic folds with wrong vergence. Thin vertical lines in both A) and B) correspond to the amounts of shortening used for the simulation snapshots in Figs. 2 and 5.

asymmetry, Fig. 7A–C shows similar snapshots to Fig. 2 (i.e., $\alpha_{ini} = 60^\circ$), but for different asymmetry shift parameters, $s = \left[\frac{1}{3} \frac{\lambda_d}{4}, \frac{1}{2} \frac{\lambda_d}{4}, \frac{2}{3} \frac{\lambda_d}{4} \right]$ (Equation (3)), and Fig. 7D shows the corresponding fold amplitude evolution curves equivalent to Fig. 6A. The amplification of the asymmetry (solid lines in Fig. 7D) during the early folding stages (up to ~18% shortening) is hardly affected by the shift. However, the de-amplification is less pronounced with increasing shift. The asymmetry situated on the larger-scale fold limb ($s = 0$) de-amplifies the most; the asymmetry close to the larger-scale fold hinge ($s = \frac{2}{3} \frac{\lambda_d}{4}$) does not de-amplify at all, but continues growing throughout the entire folding history modeled here. The other fold amplification curves shown in Fig. 7D (i.e., thin layer at larger-scale fold hinge, thick-layer) are hardly affected by the shift of the asymmetry. Hence, we could repeat the same observations as for a shift of $s = 0$ (Fig. 6A), which we however omit.

For the extreme case of ($s = \frac{2}{3} \frac{\lambda_d}{4}$) (asymmetry close to larger synformal hinge), Fig. 8 shows the effect of the initial skew angle, α_{ini} ; Fig. 8 can be directly compared to Fig. 6 showing the same data but for $s = 0$ (asymmetry centered at larger fold limb). Independent of the initial skew angle, the asymmetry continuously grows during the entire folding history (solid lines in Fig. 8A). Up to about 18% shortening, the asymmetry exhibits active growth with a growth rate similar to the true parasitic folds (dashed lines in Fig. 8A). With

increasing shortening (>18%), the growth rates of both the asymmetry and the true parasitic folds decrease corresponding to passive (pure-shear) growth until the end of the simulations. At the same time, the skew angle increases until a shortening of about 18% (Fig. 8B) corresponding to an increase in asymmetry. After about 18% shortening, the skew angle stabilizes and does not change significantly anymore. In particular, it does not decrease as for an asymmetry located on the larger-scale fold limb ($s = 0$; Fig. 6B). The other two fold amplification curves (i.e., thin layer at larger-scale fold hinge, thick-layer; Fig. 6A) are hardly affected by the shift of the asymmetry.

3.3. Combined effect of position of initial asymmetry and distance between thick layers

Figs. 6B and 8B show the skew angle evolution for the case of the two thick layers having an initial distance to each other that is equal to their thickness, H_0 (Fig. 1). To expand these results, Fig. 9 shows the effect of an increasing initial distance between the two thick layers, $[1, 1.5, 2, 3] \times H_0$ (Table 1). Despite some data scatter, which is mostly due to the initial random red noise, the general observations from above remain valid. For all studied distances between the thick layers and for both asymmetry shift parameters, $s = \left[0, \frac{2}{3} \frac{\lambda_d}{4} \right]$, the skew angle increases until a shortening of about 18%. Geometrical asymmetries located on the larger-scale fold limb

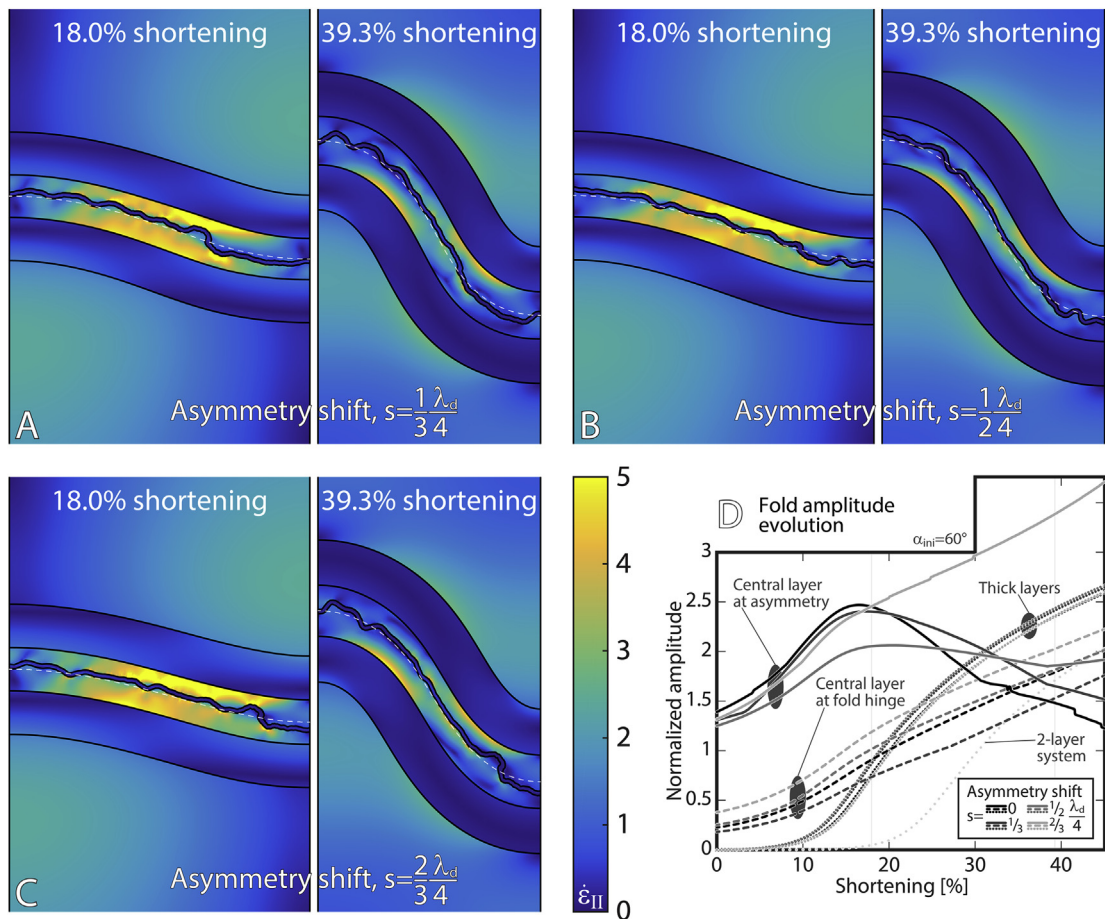


Fig. 7. A)–C) Simulation snapshots (similar to Fig. 2) of simulations with different asymmetry shift parameters, s , and initial skew angle $\alpha_{ini} = 60^\circ$. Compared to Fig. 2, only two snapshots are shown for each asymmetry shift parameter. D) Same as Fig. 6A, but for the simulations shown in A–C. Thin vertical lines correspond to the amounts of shortening used for the simulation snapshots in A–C. Note that the curves for $s = 0$ are the same as in Fig. 6A for $\alpha_{ini} = 60^\circ$.

($s = 0$; solid lines in Fig. 9) reduce their skew angle with increasing shortening and reach the initial value at a shortening of about 33%. Geometrical asymmetries located close to the larger-scale fold hinge ($s = \frac{2}{3} \frac{\lambda_d}{4}$); dashed lines in Fig. 9) stabilize their skew angle, which does not change significantly anymore with increasing shortening.

4. Discussion

We presented simplified test cases of a thin layer with a pre-existing asymmetry situated between two thicker layers. During buckle folding, the thick and thin layers develop different dominant wavelengths, λ_d and $\lambda_{d,thin}$, respectively, according to Schmid and Podladchikov (2010) and Biot (1961). Here we prescribed the larger-scale fold wavelength in the initial model setup (Equation (1)), but allowed the thin layer to develop buckle folds self-consistently using an initial random perturbation besides the prescribed asymmetry. Prior to buckling of the thick layers to finite amplitude, both the asymmetry and the random perturbation amplify. This is consistent with studies by Abbassi and Mancktelow (1990) and Adamuszek et al. (2013), which modeled the amplification of an asymmetric initial perturbation in single-layer buckle folds. However, shortly after the thick layers amplify to finite amplitude, the asymmetry de-amplifies and unfolds (Figs. 6 and 7D).

Unfolding during ongoing tectonic deformation has been investigated only in very few studies. In simple-shear deformation, Llorens et al. (2013b) demonstrated that layers, which are oriented obliquely to the shear zone boundary and within the shortening quadrant of the simple-shear flow field, rotate towards a 90°-orientation with respect to the shear zone boundary. During this rotation, the layers are shortened and develop buckle folds. If the simple-shear deformation continues, Llorens et al. (2013a) showed that the folded layers rotate away from the 90°-orientation and hence are being stretched and unfolded. This folding and unfolding happens in a constant simple-shear flow field and should not be misinterpreted as two deformation phases. Unfolding has also been investigated by Schmalholz (2008), Lechmann et al. (2010), and Frehner et al. (2012), but in pure-shear deformation. These studies applied layer-parallel extension in numerical unfolding simulations to restore folded geological layers. Hence, these studies used a time-reverse approach and did not claim that unfolding is a process actually happening in nature.

In the presented simulations, the deformation leading to unfolding of the initial asymmetry is more complex than pure or simple shear. On the larger-scale fold limb, the amplification of the larger-scale fold results in layer-perpendicular flattening (and layer-parallel extension) between the two outer thick layers (Frehner and Schmalholz, 2006). At the same time, amplification of the two outer thick layers leads to flexural flow between them (Ramsay and Huber, 1987). The resulting deformation field between the two outer thick layers is a combination of pure and simple shear. Both contributions promote unfolding of the initial asymmetry. The pure-shear component (layer-perpendicular flattening) squeezes the thin layer; the simple-shear component (flexural flow) has a rotational component opposite to the vergence of the asymmetry. This combined effect leads to a very efficient de-amplification of the asymmetry as soon as the larger-scale fold starts to grow to finite amplitude. However, both effects decrease from fold limb to fold hinge (Frehner and Schmalholz, 2006; Ramsay and Huber, 1987). Therefore, asymmetries located away from the larger-scale fold limb are less prone to de-amplification (Fig. 7, compare Figs. 6, 8 and 9).

If the asymmetry is located on the larger-scale fold limb, de-amplification begins after the larger-scale fold amplifies to finite amplitude (Figs. 6A and 7D). Therefore, de-amplification strongly depends on the initial amplitude and the growth rate of the thick layers, and ultimately also on the viscosity ratio between the higher-viscous layers and the surrounding matrix. To illustrate this, Fig. 10 shows the same fold amplification curves and skew angle development as Fig. 6, but for a viscosity ratio of $\eta_L:\eta_M = 20:1$ (as compared to $\eta_L:\eta_M = 100:1$ in Fig. 6). For this simulation, we also changed the initial model setup (Equation (2)) according to the viscosity ratio. Because such a multilayer system hardly amplifies for the given model parameters, we increased the initial amplitude of the two outer thick layers to $A_{outer} = 10^{-2}$ (as compared to $A_{outer} = 10^{-4}$ in Fig. 6). Even so, the larger-scale fold does not amplify very strongly compared to the central thin layer (Fig. 10A). Therefore, no layer-perpendicular flattening and no marked flexural flow occurs between the two outer thick layers and hence the initial asymmetry does not de-amplify. Consequently, the asymmetry is still well preserved after a shortening of 39.3% (Fig. 10D), while in the case of a viscosity ratio of $\eta_L:\eta_M = 100:1$ the asymmetry is hardly visible after the same amount of shortening (Fig. 2). This example illustrates the importance of the relationship between larger-scale and smaller-scale amplification.

Frehner and Schmalholz (2006) showed that the presence of

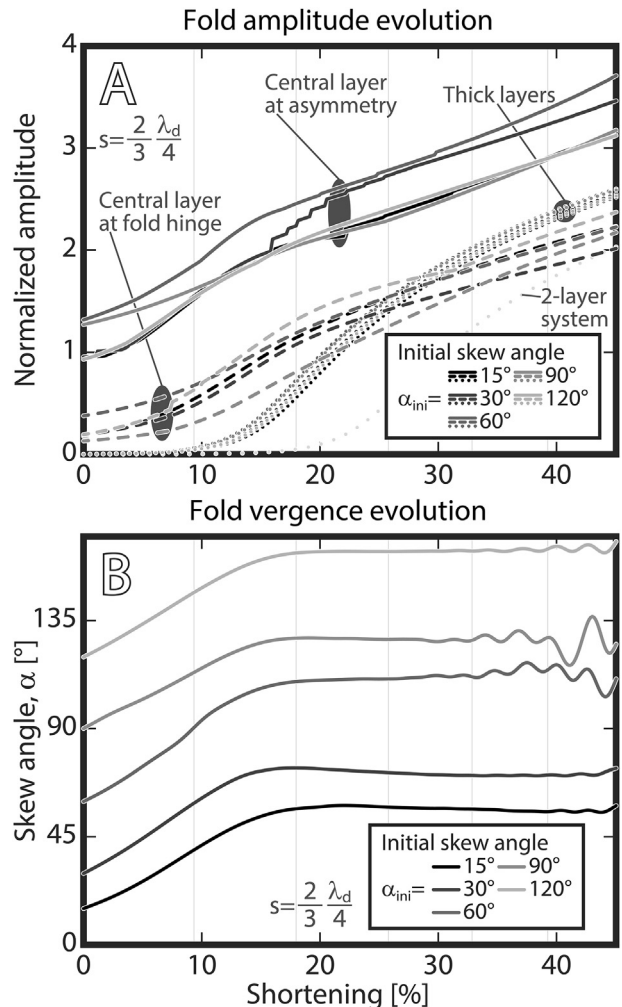


Fig. 8. Same as Fig. 6, but for an asymmetry shift parameter $s = \frac{2}{3} \frac{\lambda_d}{4}$. Note that the curves for $\alpha_{ini} = 60^\circ$ are the same as in Fig. 7D for $s = \frac{2}{3} \frac{\lambda_d}{4}$.

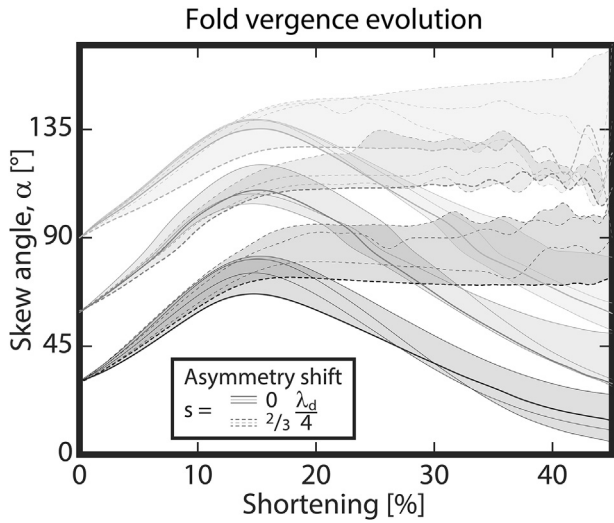


Fig. 9. Evolution of the skew angle, α , of the geometrical asymmetry as a function of increasing shortening for different initial skew angles, $\alpha_{ini} = [30^\circ, 60^\circ, 90^\circ]$ (dark to light gray), for two different asymmetry shift parameter, $s = [0, 2/3] \times \lambda_d/4$ (solid and dashed lines), and for different initial distances between the two thick layers, $[1, 1.5, 2, 3] \times H_0$ (grouped for each α_{ini} - s -combination). Slightly bolder lines correspond to data already shown in Fig. 6B (bold solid lines) and Fig. 8B (bold dashed lines).

thin layers developing parasitic folds between two thicker layers hardly influences the dynamics of the two thicker layers (Fig. 10 in Frehner and Schmalholz, 2006). However, in the presented simulations, we observe that the growth rate of the thick layers is strongly influenced by the presence of the thin layer (Figs. 6A, 7D, 8A and 10A). The only difference between the two studies is the initial geometry. It appears that the initial asymmetry of the thin layer, not the presence of the thin layer as such, modifies the larger-scale dynamics of the multilayer system. This is in general agreement with the study of Mancktelow (1999), which demonstrated that the initial geometry strongly influences the final shape of single-layer buckle folds. Naturally, various other parameters may influence the multilayer buckling dynamics (e.g., Schmid and Podladchikov, 2010; Treagus and Fletcher, 2009).

The simplified test cases presented here may not be representative for natural geological folds. In nature, a whole range of complications may occur compared to our simulations, such as more complex rheological flow laws (e.g., non-linear viscous, visco-elasto-plastic), spatially and/or temporally changing rheological behavior (e.g., different for each layer), or more complex initial geometries. However, the aim of this study was not to reproduce natural folds one-to-one, but to investigate first-order effects of pre-existing asymmetries during buckle folding and the possible inheritance of such structures. Non-linear viscous materials tend to

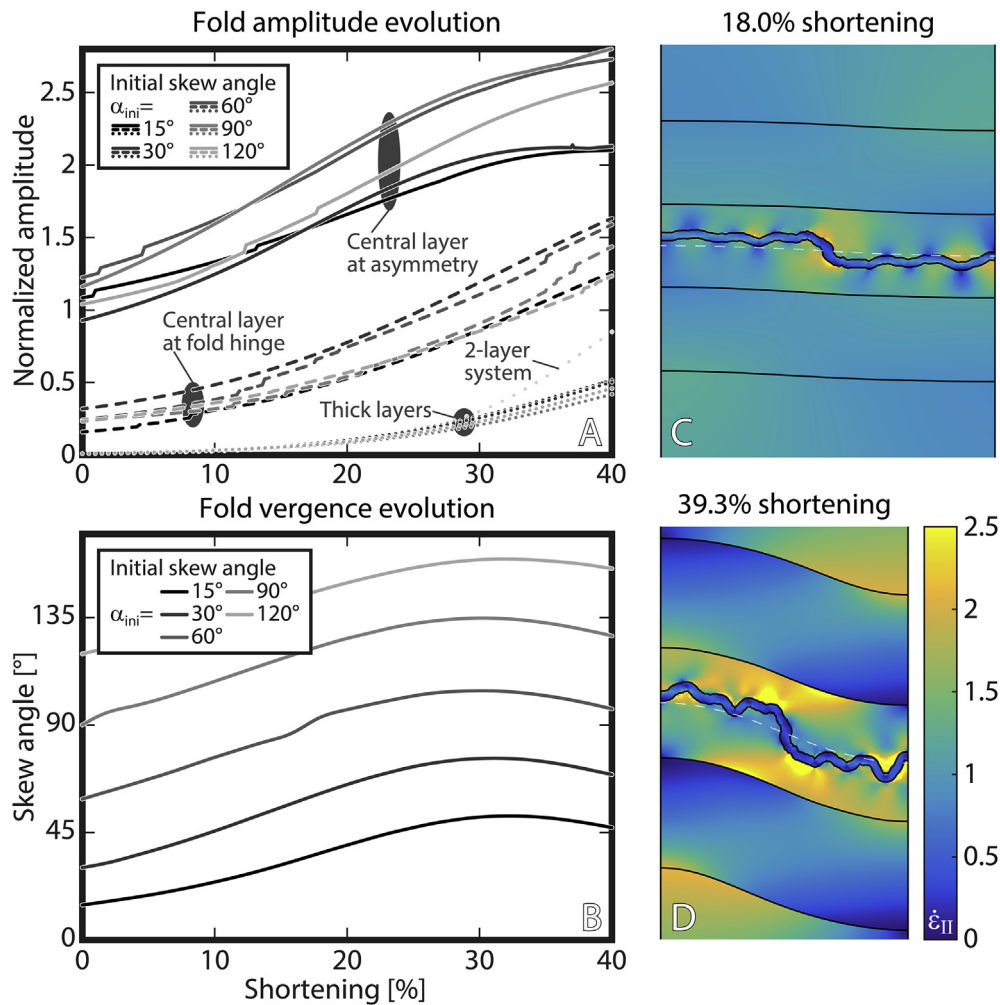


Fig. 10. A) & B) Same as Fig. 6, but for a viscosity of the higher-viscous layers of $\eta_L = 20$ (as opposed to $\eta_L = 100$ in Fig. 6) and amplitude of the two outer thick layers of $A_{outer} = 10^{-2}$ (as opposed to $A_{outer} = 10^{-4}$ in Fig. 6). C) & D) Simulation snapshots of the simulation with $\alpha_{ini} = 60^\circ$ (intermediate gray level in A & B). Note that the color scale is different compared to all other simulation snapshots (e.g., Fig. 2).

localize deformation more than linear viscous ones. The presented simulation snapshots (Figs. 2, 5, 7A–C and 10C–D) show that the strain rate is highest close to the geometrical asymmetry. For non-linear viscous materials, we therefore speculate that deformation would localize in these regions, intensifying the asymmetry compared to the presented Newtonian cases. As a result, we believe that pre-existing asymmetries in non-Newtonian materials are less prone to de-amplification and may survive buckling of the larger-scale fold more easily. However, a detailed study and quantification of the effect of rheology remains to be done in the future.

As an example for a more complex geometrical setup, Fig. 11 shows two snapshots of a simulation with 10 thin layers between the two outer thick layers. We added the initial asymmetry (Equation (3)) to all 10 layers using $\alpha_{\text{ini}} = 60^\circ$, but with a shift parameter, s , increasing from bottom to top. The initial asymmetries were therefore vertically aligned at an angle of 60° . The overall geometry of the multilayer buckle fold is quite different to the 3-layer system (Fig. 2); it resembles a much more chevron-type fold with straight limbs, sharp hinges, and hinge-collapse structures close to the inner arc of the multilayer fold. However, the evolution of the initial asymmetries is similar to the 3-layer case; they also grow first (Fig. 11, left panel) and then de-amplify (Fig. 11, right panel). The formation of a larger-scale chevron-type fold straightens the limbs even more than in the 3-layer case. Therefore, de-amplification and unfolding may be more efficient in multilayer folds compared to folds with fewer layers. However, the efficiency of de-amplification certainly also depends on the spacing between the layers, which is however not further studied here.

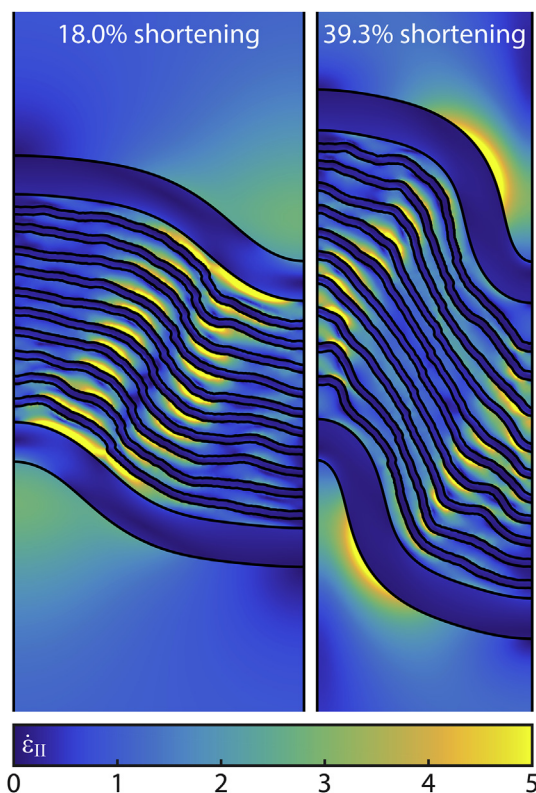


Fig. 11. Simulation snapshots of a simulation with 10 thin layers that all have an initial asymmetry with $\alpha_{\text{ini}} = 60^\circ$. The shift parameter, s , is increasing from bottom to top, so that the initial asymmetries are vertically aligned at an angle of 60° .

5. Conclusions

Whether or not a pre-existing asymmetry can be inherited during multilayer buckle folding strongly depends on the interplay between the larger-scale and smaller-scale amplification. Generally, on the limbs of the larger-scale fold two processes work against the pre-existing asymmetry: layer-perpendicular flattening and the rotational component of flexural flow. Both processes promote de-amplification and unfolding of the initial asymmetry. However, the efficiency of these two processes depends on the amplification of the larger-scale fold. If amplification is fast (i.e., large viscosity ratio $\eta_L:\eta_M$) and/or early with respect to the thin layer amplification (i.e., large initial perturbation A_{outer}), the initial asymmetry is more prone to de-amplification and unfolding.

De-amplification is a viable process on the larger-scale fold limbs during buckle folding, which may lead to unfolding and the disappearance of pre-existing structures. This is particularly true if the pre-existing folds are relatively open and exhibit low amplitudes. On the other hand, if the pre-existing fold is tight or isoclinal, its inheritance-potential may be much larger. Such tight or isoclinal folds are typical for tectonic folds, but much less frequent in sedimentary structures. Indeed, fold interference patterns of type 3 (Ramsay and Huber, 1987), which resemble parasitic folds, commonly contain isoclinal folds as their pre-existing first-phase folds. If the first-phase folds were open, they would be unfolded during the second-phase folding event and no interference pattern would ever develop.

Acknowledgements

This work is largely based on the Bachelor thesis of T. Schmid. We thank Neil Mancktelow for helpful comments and suggestions, as well as Maria-Gema Llorens and Marta Adamuszek for their valuable reviews.

References

- Abbassi, M.R., Mancktelow, N.S., 1990. The effect of initial perturbation shape and symmetry on fold development. *J. Struct. Geol.* 12, 273–282. [http://dx.doi.org/10.1016/0191-8141\(90\)90011-M](http://dx.doi.org/10.1016/0191-8141(90)90011-M).
- Adamuszek, M., Schmid, D.W., Dabrowski, M., 2013. Theoretical analysis of large amplitude folding of a single viscous layer. *J. Struct. Geol.* 48, 137–152. <http://dx.doi.org/10.1016/j.jsg.2012.11.006>.
- Biot, M.A., 1961. Theory of folding of stratified viscoelastic media and its implications in tectonics and orogenesis. *Geol. Soc. Am. Bull.* 72–1620. [http://dx.doi.org/10.1130/0016-7606\(1961\)72\[1595:T0FOSV\]2.0.CO;2](http://dx.doi.org/10.1130/0016-7606(1961)72[1595:T0FOSV]2.0.CO;2).
- Cuvelier, C., Segal, A.A., van Steenhoven, A.A., 1986. *Finite Element Methods and Navier-Stokes Equations*. D. Reidel Publishing Company, Dordrecht.
- De Sitter, L.U., 1958. Boudins and parasitic folds in relation to cleavage and folding. *Geol. Mijnb.* 20, 277–286.
- Deubelbeiss, Y., Kaus, B.J.P., 2008. Comparison of Eulerian and Lagrangian numerical techniques for the Stokes equations in the presence of strongly varying viscosity. *Phys. Earth Planet. Interiors* 171, 92–111. <http://dx.doi.org/10.1016/j.pepi.2008.06.023>.
- Duncan, I.J., 1984. Structural evolution of the Thor-Odin gneiss dome. *Tectonophysics* 101, 87–130. [http://dx.doi.org/10.1016/0040-1951\(84\)90044-1](http://dx.doi.org/10.1016/0040-1951(84)90044-1).
- Fletcher, R.C., 1977. Folding of a single viscous layer: exact infinitesimal-amplitude solution. *Tectonophysics* 39, 593–606. [http://dx.doi.org/10.1016/0040-1951\(77\)90155-X](http://dx.doi.org/10.1016/0040-1951(77)90155-X).
- Fossen, H., 2010. *Structural Geology*. Cambridge University Press, Cambridge.
- Frehner, M., 2011. The neutral lines in buckle folds. *J. Struct. Geol.* 33, 1501–1508. <http://dx.doi.org/10.1016/j.jsg.2011.07.005>.
- Frehner, M., Reif, D., Grasemann, B., 2012. Mechanical versus kinematical shortening reconstructions of the Zagros high folded zone (Kurdistan region of Iraq). *Tectonics* 31, TC3002. <http://dx.doi.org/10.1029/2011TC003010>.
- Frehner, M., Schmalholz, S.M., 2006. Numerical simulations of parasitic folding in multilayers. *J. Struct. Geol.* 28, 1647–1657. <http://dx.doi.org/10.1016/j.jsg.2006.05.008>.
- Froitzheim, N., Schmid, S.M., Conti, P., 1994. Repeated change from crustal shortening to orogen-parallel extension in the Austroalpine units of Graubünden. *Eclogae Geol. Helv.* 87, 559–612. <http://dx.doi.org/10.5169/seals-167471>.
- Harrison, J.V., Falcon, N.L., 1934. Collapse structures. *Geol. Mag.* 71, 529–539. <http://dx.doi.org/10.1017/S0016756800095005>.

- Hunt, G.W., Wade, M.A., Ord, A., 2001. Length scale interactions in the folding of sandwich structures. *Tectonophysics* 335, 111–120. [http://dx.doi.org/10.1016/S0040-1951\(01\)00051-8](http://dx.doi.org/10.1016/S0040-1951(01)00051-8).
- Lechmann, S.M., Schmalholz, S.M., Burg, J.-P., Marques, F.O., 2010. Dynamic unfolding of multilayers: 2D numerical approach and application to turbidites in SW Portugal. *Tectonophysics* 494, 64–74. <http://dx.doi.org/10.1016/j.tecto.2010.08.009>.
- Llorens, M.-G., Bons, P.D., Griera, A., Gomez-Rivas, E., 2013a. When do folds unfold during progressive shear? *Geology* 41, 563–566. <http://dx.doi.org/10.1130/G33973.1>.
- Llorens, M.-G., Bons, P.D., Griera, A., Gomez-Rivas, E., Evans, L.A., 2013b. Single layer folding in simple shear. *J. Struct. Geol.* 50, 209–220. <http://dx.doi.org/10.1016/j.jsg.2012.04.002>.
- Mancktelow, N.S., 1999. Finite-element modelling of single-layer folding in elastoviscous materials: the effect of initial perturbation geometry. *J. Struct. Geol.* 21, 161–177. [http://dx.doi.org/10.1016/S0191-8141\(98\)00102-3](http://dx.doi.org/10.1016/S0191-8141(98)00102-3).
- Pleuger, J., Nagel, T.J., Walter, J.M., Jansen, E., Froitzheim, N., 2008. On the role and importance of orogen-parallel and -perpendicular extension, transcurrent shearing, and backthrusting in the Monte Rosa nappe and the Southern Steep Belt of the Alps (Penninic zone, Switzerland and Italy). *Geol. Soc. Lond.* 298, 251–280. <http://dx.doi.org/10.1144/SP298.13>. Special Publications.
- Price, N.J., Cosgrove, J.W., 1990. *Analysis of Geological Structures*. Cambridge University Press, Cambridge.
- Pumpelly, R., Wolff, J.E., Dale, T.N., 1894. *Geology of the Green Mountains in Massachusetts*. U.S. Geological Survey Monograph 23.
- Ramberg, H., 1964. Selective buckling of composite layers with contrasted rheological properties, a theory for simultaneous formation of several orders of folds. *Tectonophysics* 1, 307–341. [http://dx.doi.org/10.1016/0040-1951\(64\)90020-4](http://dx.doi.org/10.1016/0040-1951(64)90020-4).
- Ramberg, H., 1963. Evolution of drag folds. *Geol. Mag.* 100, 97–106. <http://dx.doi.org/10.1017/S0016756800055321>.
- Ramsay, J.G., Huber, M.I., 1987. *The techniques of modern structural geology. In: Folds and Fractures, vol. 2*. Academic Press, London.
- Schmalholz, S.M., 2008. 3D numerical modeling of forward folding and reverse unfolding of a viscous single-layer: implications for the formation of folds and fold patterns. *Tectonophysics* 446, 31–41. <http://dx.doi.org/10.1016/j.tecto.2007.09.005>.
- Schmalholz, S.M., Schmid, D.W., 2012. Folding in power-law viscous multi-layers. *Philos. Trans. R. Soc. A Math. Phys. Eng. Sci.* 370, 1798–1826. <http://dx.doi.org/10.1098/rsta.2011.0421>.
- Schmid, D.W., Podladchikov, Y.Y., 2010. Fold amplification rates and dominant wavelength selection in multilayer stacks. *Philos. Mag.* 86, 3409–3423. <http://dx.doi.org/10.1080/14786430500380175>.
- Treagus, S.H., Fletcher, R.C., 2009. Controls of folding on different scales in multilayered rocks. *J. Struct. Geol.* 31, 1340–1349. <http://dx.doi.org/10.1016/j.jsg.2009.07.009>.
- Twiss, R.J., Moores, E.M., 2007. *Structural Geology*. W. H. Freeman and Company, New York.
- Van der Pluijm, B.A., Marshak, S., 2004. *Earth Structure: an Introduction to Structural Geology and Tectonics*, second ed. W. W. Norton & Company, Inc., New York.
- Williams, E., 1961. The deformation of confined, incompetent layers in folding. *Geol. Mag.* 98, 317–323. <http://dx.doi.org/10.1017/S0016756800060647>.
- Zienkiewicz, O.C., Taylor, R.L., 2000. *The finite element method. In: The Basis, vol. 1*. Butterworth-Heinemann, Oxford.